Wilhelm Burger · Mark J. Burge

Digital Image Processing

An algorithmic introduction using Java

Second Edition

ERRATA

Springer
Berlin Heidelberg NewYork
HongKong London
Milano Paris Tokyo

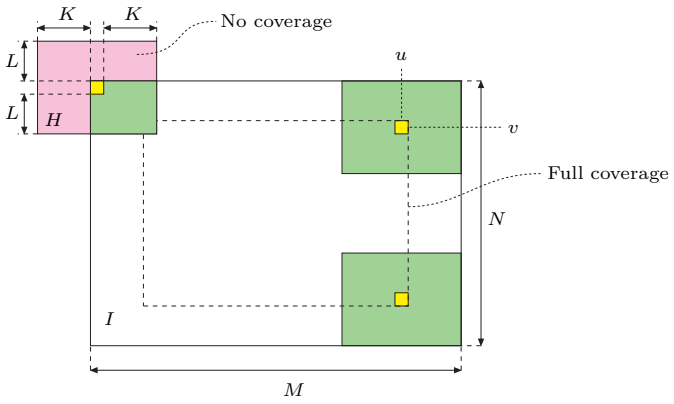

Fig. 5.7 Border geometry. The filter can be applied only at locations where the kernel H of size $(2K+1) \times (2L+1)$ is fully contained in the image (inner rectangle).

of key importance in practice: smoothing filters and difference filters (Fig. 5.8).

Smoothing filters

Every filter we have discussed so far causes some kind of smoothing. In fact, any linear filter with positive-only coefficients is a smoothing filter in a sense, because such a filter computes merely a weighted average of the image pixels within a certain image region.

Box filter

This simplest of all smoothing filters, whose 3D shape resembles a box (Fig. 5.8(a)), is a well-known friend already. Unfortunately, the box filter is far from an optimal smoothing filter due to its wild behavior in frequency space, which is caused by the sharp cutoff around its sides. Described in frequency terms, smoothing corresponds to low-pass filtering, that is, effectively attenuating all signal components above a given cutoff frequency (see also Chs. 18–19). The box filter, however, produces strong "ringing" in frequency space and is therefore not considered a high-quality smoothing filter. It may also appear rather ad hoc to assign the same weight to all image pixels in the filter region. Instead, one would probably expect to have stronger emphasis given to pixels near the center of the filter than to the more distant ones. Furthermore, smoothing filters should possibly operate "isotropically" (i.e., uniformly in each direction), which is certainly not the case for the rectangular box filter.

Gaussian filter

The filter matrix (Fig. 5.8(b)) of this smoothing filter corresponds to a 2D Gaussian function,

$$H^{\mathrm{G},\sigma}(x,y) = e^{-\frac{x^2+y^2}{2\sigma^2}} = e^{-\frac{r^2}{2\sigma^2}}, \tag{5.14}$$

where σ denotes the width (standard deviation) of the bell-shaped function and r is the distance (radius) from the center. The pixel at the center receives the maximum weight (1.0, which is scaled to the integer value 9 in the matrix shown in Fig. 5.8(b)), and the remaining coefficients drop off smoothly with increasing distance from the

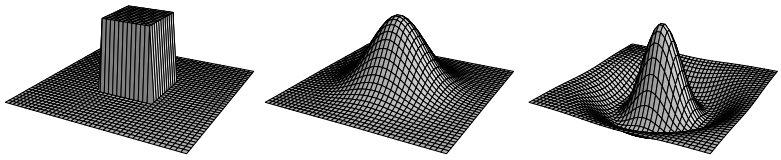

$$\frac{1}{9}\cdot\begin{bmatrix} 0 & 0 & 0 & 0 & 0 \\ 0 & 1 & 1 & 1 & 0 \\ 0 & 1 & 1 & 1 & 0 \\ 0 & 1 & 1 & 1 & 0 \\ 0 & 0 & 0 & 0 & 0 \end{bmatrix} \quad \frac{1}{57}\cdot\begin{bmatrix} 0 & 1 & 2 & 1 & 0 \\ 1 & 3 & 5 & 3 & 1 \\ 2 & 5 & 9 & 5 & 2 \\ 1 & 3 & 5 & 3 & 1 \\ 0 & 1 & 2 & 1 & 0 \end{bmatrix} \quad \frac{1}{16}\cdot\begin{bmatrix} 0 & 0 & -1 & 0 & 0 \\ 0 & -1 & -2 & -1 & 0 \\ -1 & -2 & 16 & -2 & -1 \\ 0 & -1 & -2 & -1 & 0 \\ 0 & 0 & -1 & 0 & 0 \end{bmatrix}$$

(a) (b) (c)

Fig. 5.8
Typical examples of linear filters, illustrated as 3D plots (top), ~~profiles (center),~~ and approximations by discrete filter matrices (bottom). The "box" filter (a) and the Gauss filter (b) are both *smoothing filters* with all-positive coefficients. The "Laplacian" or "Mexican hat" filter (c) is a *difference filter*. It computes the weighted difference between the center pixel and the surrounding pixels and thus reacts most strongly to local intensity peaks.

center. The Gaussian filter is isotropic if the discrete filter matrix is large enough for a sufficient approximation (at least 5×5). As a low-pass filter, the Gaussian is "well-behaved" in frequency space and thus clearly superior to the box filter. The 2D Gaussian filter is separable into a pair of 1D filters (see Sec. 5.3.3), which facilitates its efficient implementation.[2]

Difference filters

If some of the filter coefficients are negative, the filter calculation can be interpreted as the difference of two sums: the weighted sum of all pixels with associated positive coefficients minus the weighted sum of pixels with negative coefficients in the filter region R_H, that is,

$$I'(u,v) = \sum_{(i,j)\in R^+} I(u+i,v+j)\cdot|H(i,j)| - \sum_{(i,j)\in R^-} I(u+i,v+j)\cdot|H(i,j)|\,, \tag{5.15}$$

where R_H^+ and R_H^- denote the partitions of the filter with positive coefficients $H(i,j) > 0$ and negative coefficients $H(i,j) < 0$, respectively. For example, the 5×5 Laplace filter in Fig. 5.8(c) computes the difference between the center pixel (with weight 16) and the weighted sum of 12 surrounding pixels (with weights -1 or -2). The remaining 12 pixels have associated zero coefficients and are thus ignored in the computation.

While local intensity variations are *smoothed* by averaging, we can expect the exact contrary to happen when differences are taken: local intensity changes are *enhanced*. Important applications of difference filters thus include edge detection (Sec. 6.2) and image sharpening (Sec. 6.6).

5.3 Formal Properties of Linear Filters

In the previous sections, we have approached the concept of filters in a rather casual manner to quickly get a grasp of how filters are defined and used. While such a level of treatment may be sufficient for most practical purposes, the power of linear filters may not really

[2] See also Sec. E in the Appendix.

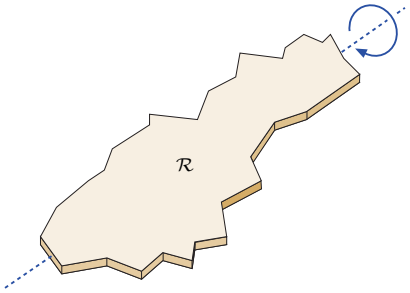

Fig. 10.17 Major axis of a region. Rotating an elongated region $\mathcal{R}$, interpreted as a physical body, around its major axis requires less effort (least moment of inertia) than rotating it around any other axis.

the pencil exhibits the least mass inertia (Fig. 10.17). As long as a region exhibits an orientation at all (i.e., $\mu_{11}(\mathcal{R}) \neq 0$), the direction $\theta_\mathcal{R}$ of the major axis can be found directly from the central moments μ_{pq} as

$$\tan(2\,\theta_\mathcal{R}) = \frac{2 \cdot \mu_{11}(\mathcal{R})}{\mu_{20}(\mathcal{R}) - \mu_{02}(\mathcal{R})} \tag{10.27}$$

and thus the corresponding angle is

$$\theta_\mathcal{R} = \frac{1}{2} \cdot \tan^{-1}\Big(\frac{2 \cdot \mu_{11}(\mathcal{R})}{\mu_{20}(\mathcal{R}) - \mu_{02}(\mathcal{R})}\Big) \tag{10.28}$$

$$= \frac{1}{2} \cdot \mathrm{ArcTan}\big(\mu_{20}(\mathcal{R}) - \mu_{02}(\mathcal{R}), 2 \cdot \mu_{11}(\mathcal{R})\big). \tag{10.29}$$

The resulting angle $\theta_\mathcal{R}$ is in the range $[-\frac{\pi}{2}, \frac{\pi}{2}]$.[9] Orientation measurements based on region moments are very accurate in general.

Calculating orientation vectors

When visualizing region properties, a frequent task is to plot the region's orientation as a line or arrow, usually anchored at the center of gravity $\bar{\boldsymbol{x}} = (\bar{x}, \bar{y})^\mathsf{T}$; for example, by a parametric line of the form

$$\boldsymbol{x} = \bar{\boldsymbol{x}} + \lambda \cdot \boldsymbol{x}_\mathrm{d} = \begin{pmatrix} \bar{x} \\ \bar{y} \end{pmatrix} + \lambda \cdot \begin{pmatrix} \cos(\theta_\mathcal{R}) \\ \sin(\theta_\mathcal{R}) \end{pmatrix}, \tag{10.30}$$

with the normalized orientation vector $\boldsymbol{x}_\mathrm{d}$ and the length variable $\lambda > 0$. To find the unit orientation vector $\boldsymbol{x}_d = (\cos\theta, \sin\theta)^\mathsf{T}$, we could first compute the inverse tangent to get 2θ (Eqn. (10.28)) and then compute the cosine and sine of θ. However, the vector $\boldsymbol{x}_d$ can also be obtained without using trigonometric functions as follows. Rewriting Eqn. (10.27) as

$$\tan(2\theta_\mathcal{R}) = \frac{2 \cdot \mu_{11}(\mathcal{R})}{\mu_{20}(\mathcal{R}) - \mu_{02}(\mathcal{R})} = \frac{a}{b} = \frac{\sin(2\theta_\mathcal{R})}{\cos(2\theta_\mathcal{R})}, \tag{10.31}$$

we get (by Pythagora's theorem)

[9] See Sec. A.1 in the Appendix for the computation of angles with the ArcTan() (inverse tangent) function and Sec. F.1.6 for the corresponding Java method `Math.atan2()`.

In practice, the logarithm of these quantities (that is, $\log(\phi_k)$) is used since the raw values may have a very large range. These features are also known as *moment invariants* since they are invariant under translation, rotation, and scaling. While defined here for binary images, they are also applicable to parts of grayscale images; examples can be found in [88, p. 517].

Flusser's invariant moments

It was shown in [72,73] that Hu's moments, as listed in Eqn. (10.47), are partially redundant and incomplete. Based on so-called *complex moments* $c_{pq} \in \mathbb{C}$, Flusser designed an improved set of 11 rotation and scale-invariant features $\psi_1, \ldots, \psi_{11}$ (see Eqn. (10.51)) for characterizing 2D shapes. For grayscale images (with $I(u,v) \in \mathbb{R}$), the complex moments of order p, q are defined as

$$c_{p,q}(\mathcal{R}) = \sum_{(u,v)\in\mathcal{R}} I(u,v) \cdot (u + \mathrm{i}\cdot v)^p \cdot (u - \mathrm{i}\cdot v)^q, \tag{10.48}$$

with centered positions $x = u - \bar{x}$ and $y = v - \bar{y}$, and $(\bar{x}, \bar{y})$ being the *centroid* of $\mathcal{R}$ (i denotes the imaginary unit). In the case of binary images (with $I(u,v) \in [0,1]$) Eqn. (10.48) simplifies to

$$c_{p,q}(\mathcal{R}) = \sum_{(u,v)\in\mathcal{R}} (u + \mathrm{i}\cdot v)^p \cdot (u - \mathrm{i}\cdot v)^q. \tag{10.49}$$

Analogous to Eqn. (10.26), the complex moments can be *scale-normalized* to

$$\hat{c}_{p,q}(\mathcal{R}) = \frac{1}{A^{(p+q+2)/2}} \cdot c_{p,q}(\mathcal{R}), \tag{10.50}$$

with A being the area of $\mathcal{R}$ [74, p. 29]. Finally, the derived rotation and scale invariant region moments of 2nd to 4th order are[15]

$$\begin{aligned}
\psi_1 &= \mathrm{Re}(\hat{c}_{1,1}), & \psi_2 &= \mathrm{Re}(\hat{c}_{2,1}\cdot\hat{c}_{1,2}), & \psi_3 &= \mathrm{Re}(\hat{c}_{2,0}\cdot\hat{c}_{1,2}^2),\\
\psi_4 &= \mathrm{Im}(\hat{c}_{2,0}\cdot\hat{c}_{1,2}^2), & \psi_5 &= \mathrm{Re}(\hat{c}_{3,0}\cdot\hat{c}_{1,2}^3), & \psi_6 &= \mathrm{Im}(\hat{c}_{3,0}\cdot\hat{c}_{1,2}^3),\\
\psi_7 &= \mathrm{Re}(\hat{c}_{2,2}), & \psi_8 &= \mathrm{Re}(\hat{c}_{3,1}\cdot\hat{c}_{1,2}^2), & \psi_9 &= \mathrm{Im}(\hat{c}_{3,1}\cdot\hat{c}_{1,2}^2),\\
\psi_{10} &= \mathrm{Re}(\hat{c}_{4,0}\cdot\hat{c}_{1,2}^4), & \psi_{11} &= \mathrm{Im}(\hat{c}_{4,0}\cdot\hat{c}_{1,2}^4).
\end{aligned} \tag{10.51}$$

Table 10.1 lists the normalized Flusser moments for five binary shapes taken from the Kimia dataset [134].

Shape matching with region moments

One obvious use of invariant region moments is shape matching and classification. Given two binary shapes A and B, with associated moment ("feature") vectors

$$\boldsymbol{f}_A = (\psi_1(A), \ldots, \psi_{11}(A)) \quad \text{and} \quad \boldsymbol{f}_B = (\psi_1(B), \ldots, \psi_{11}(B)),$$

respectively, one approach could be to simply measure the difference between shapes by the Euclidean distance of these vectors in the form

[15] In Eqn. (10.51), the use of Re( ) for the quantities ψ_1, ψ_2, ψ_7 (which are real-valued *per se*) is redundant.

RGB

R *G* *B*

Fig. 12.2
A color image and its corresponding RGB channels. The fruits depicted are mainly yellow and red and therefore have high values in the R and G channels. In these regions, the B content is correspondingly lower (represented here by darker gray values) except for the bright highlights on the apple, where the color changes gradually to white. The tabletop in the foreground is purple and therefore displays correspondingly higher values in its B channel.

individual color components. In the next sections we will examine the difference between *true color* images, which utilize colors uniformly selected from the entire color space, and so-called *palleted* or *indexed* images, in which only a select set of distinct colors are used. Deciding which type of image to use depends on the requirements of the application.

Duplicate text removed.

True color images

A pixel in a true color image can represent any color in its color space, as long as it falls within the (discrete) range of its individual color components. True color images are appropriate when the image contains many colors with subtle differences, as occurs in digital photography and photo-realistic computer graphics. Next we look at two methods of ordering the color components in true color images: *component ordering* and *packed ordering*.

in Chapter 12, Sec. 12.2.1, where we had simply ignored the issue of possible nonlinearities. As one may have guessed, however, the variables R, G, B, and Y in Eqn. (12.10) on p. 305,

$$Y = 0.2125 \cdot R + 0.7154 \cdot G + 0.072 \cdot B \tag{14.37}$$

implicitly refer to *linear* color and gray values, respectively, and not the raw sRGB values! Based on Eqn. (14.37), the *correct* grayscale conversion from raw (nonlinear) sRGB components R', G', B' is

$$Y' = f_1\big(0.2125 \cdot f_2(R') + 0.7154 \cdot f_2(G') + 0.0721 \cdot f_2(B')\big), \tag{14.38}$$

with $f_1()$ and $f_2()$ as defined in Eqns. (14.33) and (14.35), respectively. The result (Y') is again a nonlinear, sRGB-compatible gray value; that is, the sRGB color tuple (Y', Y', Y') should have the same perceived luminance as the original color (R', G', B').

Note that setting the components of an sRGB color pixel to three arbitrary but identical values Y',

$$(R', G', B') \leftarrow (Y', Y', Y')$$

always creates a gray (colorless) pixel, despite the nonlinearities of the sRGB space. This is due to the fact that the gamma correction (Eqns. (14.33) and (14.35)) applies evenly to all three color components and thus any three identical values map to a (linearized) color on the straight gray line between the black point **S** and the white point **W** in XYZ space (cf. Fig. 14.1(b)).

For many applications, however, the following *approximation* to the exact grayscale conversion in Eqn. (14.38) is sufficient. It works without converting the sRGB values (i.e., directly on the nonlinear R', G', B' components) by computing a linear combination

$$Y' \approx w'_R \cdot R' + w'_G \cdot G' + w'_B \cdot B', \tag{14.39}$$

with a slightly different set of weights; for example, $w'_R = 0.309$, $w'_G = 0.609$, $w'_B = 0.082$, as proposed in [188]. The resulting quantity from Eqn. (14.39) is sometimes called *luma* (compared to *luminance* in Eqn. (14.37)).

14.5 Adobe RGB

A distinct weakness of sRGB is its relatively small gamut, which is limited to the range of colors reproducible by ordinary color monitors. This causes problems, for example, in printing, where larger gamuts are needed, particularly in the green regions. The "Adobe RGB (1998)" [1] color space, developed by Adobe as their own standard, is based on the same general concept as sRGB but exhibits a significantly larger gamut (Fig. 14.3), which extends its use particularly to print applications. Figure 14.7 shows the noted difference between the sRGB and Adobe RGB gamuts in 3D CIEXYZ color space.

The neutral point of Adobe RGB corresponds to the D65 standard (with $x = 0.3127$, $y = 0.3290$), and the gamma value is 2.199

$$I'(u,v) \leftarrow \sum_{m=-\infty}^{\infty} \sum_{n=-\infty}^{\infty} I(u+m, v+n) \cdot H_{\mathrm{d}}(m,n) \tag{17.15}$$

$$= \sum_{i=-\infty}^{\infty} \sum_{j=-\infty}^{\infty} I(i,j) \cdot H_{\mathrm{d}}(i-u, j-v), \tag{17.16}$$

every new pixel value $I'(u,v)$ is the weighted average of the original image pixels I in a certain neighborhood, with the weights specified by the elements of the filter kernel H_{d}.[5] The weight assigned to each pixel only depends on its spatial position relative to the current center coordinate (u,v). In particular, $H_{\mathrm{d}}(0,0)$ specifies the weight of the center pixel $I(u,v)$, and $H_{\mathrm{d}}(m,n)$ is the weight assigned to a pixel displaced by (m,n) from the center. Since only the spatial image coordinates are relevant, such a filter is called a *domain filter*. Obviously, ordinary filters as we know them are *all* domain filters.

17.2.2 Range Filter

Although the idea may appear strange at first, one could also apply a linear filter to the pixel *values* or *range* of an image in the form

$$I'_r(u,v) \leftarrow \sum_{i=-\infty}^{\infty} \sum_{j=-\infty}^{\infty} I(i,j) \cdot H_{\mathrm{r}}\big(I(i,j) - I(u,v)\big). \tag{17.17}$$

The contribution of each pixel is specified by the function H_{r} and depends on the difference between its own *value* $I(i,j)$ and the value at the current center pixel $I(u,v)$. The operation in Eqn. (17.17) is called a *range filter*, where the spatial position of a contributing pixel is irrelevant and only the difference in values is considered. For a given position (u,v), all surrounding image pixels $I(i,j)$ with the same value contribute equally to the result $I'_r(u,v)$. Consequently, the application of a *range* filter has no *spatial* effect upon the image—in contrast to a *domain* filter, no blurring or sharpening will occur. Instead, a range filter effectively performs a global *point operation* by remapping the intensity or color values. However, a global *range filter* by itself is of little use, since it combines pixels from the entire image and only changes the intensity or color map of the image, equivalent to a nonlinear, image-dependent point operation.

17.2.3 Bilateral Filter—General Idea

The key idea behind the bilateral filter is to *combine* domain filtering (Eqn. (17.16)) *and* range filtering (Eqn. (17.17)) in the form

$$I'(u,v) = \frac{1}{W_{u,v}} \cdot \sum_{i=-\infty}^{\infty} \sum_{j=-\infty}^{\infty} I(i,j) \cdot \underbrace{H_{\mathrm{d}}(i-u, j-v) \cdot H_{\mathrm{r}}\big(I(i,j) - I(u,v)\big)}_{w_{i,j}}, \tag{17.18}$$

[5] In Eqn. (17.16), functions I and H_{d} are assumed to be zero outside their domains of definition.

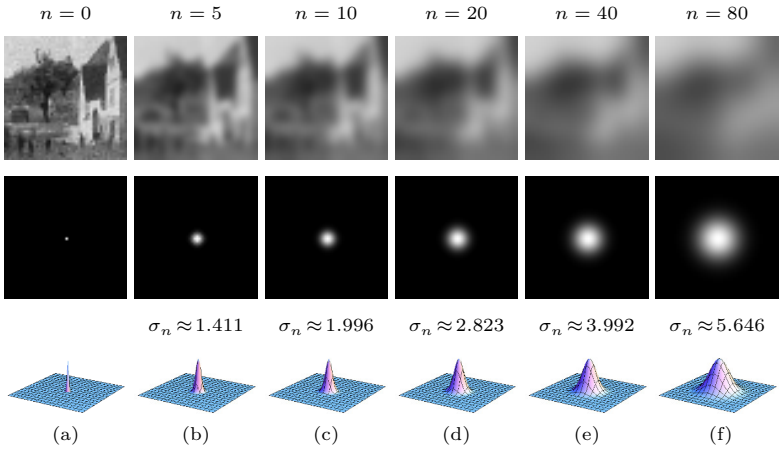

Fig. 17.15
Discrete isotropic diffusion. Blurred images and impulse response obtained after n iterations, with $\alpha = 0.20$ (see Eqn. (17.45)). The size of the images is 50×50. The width of the equivalent Gaussian kernel (σ_n) grows with the square root of n (the number of iterations). Impulse response plots are normalized to identical peak values.

$$I^{(n)}(\boldsymbol{u}) \leftarrow \begin{cases} I(\boldsymbol{u}) & \text{for } n = 0, \\ I^{(n-1)}(\boldsymbol{u}) + \alpha \cdot \left[\nabla^2 I^{(n-1)}(\boldsymbol{u})\right] & \text{for } n > 0, \end{cases} \tag{17.45}$$

for each image position $\boldsymbol{u} = (u, v)$, with n denoting the iteration number. This is called the "direct" solution method (there are other methods but this is the simplest). The constant α in Eqn. (17.45) is the time increment, which controls the speed of the diffusion process. Its value should be in the range $(0, 0.25]$ for the numerical scheme to be stable. At each iteration n, the variations in the image function are reduced and (depending on the boundary conditions) the image function should eventually flatten out to a constant plane as n approaches infinity.

For a discrete image I, the Laplacian $\nabla^2 I$ in Eqn. (17.45) can be approximated by a linear 2D filter,

$$\nabla^2 I \approx I * H^L, \qquad \text{with } H^L = \begin{bmatrix} 0 & 1 & 0 \\ 1 & -4 & 1 \\ 0 & 1 & 0 \end{bmatrix}, \tag{17.46}$$

as described earlier.[11] An essential property of isotropic diffusion is that it has the same effect as a Gaussian filter whose width grows with the elapsed time. For a discrete 2D image, in particular, the result obtained after n diffusion steps (Eqn. (17.45)), is the same as applying a linear filter to the original image I,

$$I^{(n)} \equiv I * H^{\mathrm{G},\sigma_n}, \tag{17.47}$$

with the normalized Gaussian kernel

$$H^{\mathrm{G},\sigma_n}(x, y) = \frac{1}{2\pi\sigma_n^2} \cdot e^{-\frac{x^2+y^2}{2\sigma_n^2}} \tag{17.48}$$

of width $\sigma_n = \sqrt{2t} = \sqrt{2n \cdot \alpha}$. The example in Fig. 17.15 illustrates this Gaussian smoothing behavior obtained with discrete isotropic diffusion.

[11] See also Chapter 6, Sec. 6.6.1 and Sec. C.3.1 in the Appendix.

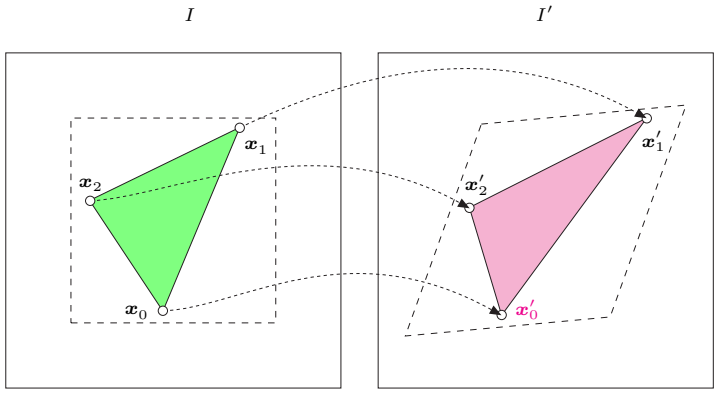

Fig. 21.2
Affine mapping. An affine 2D transformation is uniquely specified by three pairs of corresponding points; for example, $(\boldsymbol{x}_0, \boldsymbol{x}'_0)$, $(\boldsymbol{x}_1, \boldsymbol{x}'_1)$, and $(\boldsymbol{x}_2, \boldsymbol{x}'_2)$.

six transformation parameters $a_{00}, \ldots, a_{12}$ are derived by solving the system of linear equations

$$\begin{aligned} x'_0 &= a_{00}\cdot x_0 + a_{01}\cdot y_0 + a_{02}, \qquad & y'_0 &= a_{10}\cdot x_0 + a_{11}\cdot y_0 + a_{12},\\ x'_1 &= a_{00}\cdot x_1 + a_{01}\cdot y_1 + a_{02}, \qquad & y'_1 &= a_{10}\cdot x_1 + a_{11}\cdot y_1 + a_{12},\\ x'_2 &= a_{00}\cdot x_2 + a_{01}\cdot y_2 + a_{02}, \qquad & y'_2 &= a_{10}\cdot x_2 + a_{11}\cdot y_2 + a_{12}, \end{aligned} \tag{21.25}$$

provided that the points (vectors) $\boldsymbol{x}_0$, $\boldsymbol{x}_1$, $\boldsymbol{x}_2$ are linearly independent (i.e., that they do not lie on a common straight line). Since Eqn. (21.25) consists of two independent sets of linear 3×3 equations for x'_i and y'_i, the solution can be written in closed form as

$$\begin{aligned} a_{00} &= \tfrac{1}{d}\cdot[y_0(x'_1 - x'_2) &&+ y_1(x'_2 - x'_0) &&+ y_2(x'_0 - x'_1)],\\ a_{01} &= \tfrac{1}{d}\cdot[x_0(x'_2 - x'_1) &&+ x_1(x'_0 - x'_2) &&+ x_2(x'_1 - x'_0)],\\ a_{10} &= \tfrac{1}{d}\cdot[y_0(y'_1 - y'_2) &&+ y_1(y'_2 - y'_0) &&+ y_2(y'_0 - y'_1)],\\ a_{11} &= \tfrac{1}{d}\cdot[x_0(y'_2 - y'_1) &&+ x_1(y'_0 - y'_2) &&+ x_2(y'_1 - y'_0)],\\ a_{02} &= \tfrac{1}{d}\cdot[x_0(y_2x'_1 - y_1x'_2) &&+ x_1(y_0x'_2 - y_2x'_0) &&+ x_2(y_1x'_0 - y_0x'_1)],\\ a_{12} &= \tfrac{1}{d}\cdot[x_0(y_2y'_1 - y_1y'_2) &&+ x_1(y_0y'_2 - y_2y'_0) &&+ x_2(y_1y'_0 - y_0y'_1)], \end{aligned} \tag{21.26}$$

with $d = x_0(y_2 - y_1) + x_1(y_0 - y_2) + x_2(y_1 - y_0)$.

Inverse affine mapping

The inverse of the affine transformation, which is often required in practice (see Sec. 21.2.2), can be calculated by simply applying the inverse of the transformation matrix $\mathbf{A}_{\text{affine}}$ (Eqn. (21.20)) in homogeneous coordinate space, that is,

$$\underline{\boldsymbol{x}} = \mathbf{A}_{\text{affine}}^{-1} \cdot \underline{\boldsymbol{x}}' \tag{21.27}$$

or $\boldsymbol{x} = \text{hom}^{-1}\left[\mathbf{A}_{\text{affine}}^{-1} \cdot \text{hom}(\boldsymbol{x}')\right]$ in Cartesian coordinates, that is,

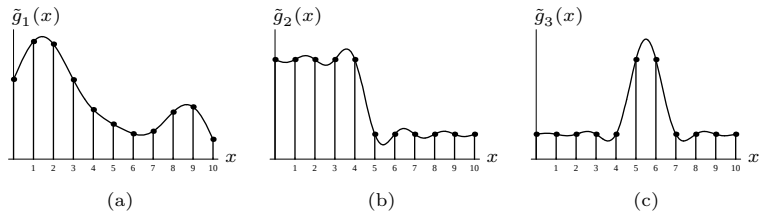

Fig. 22.6
Sinc interpolation applied to various signal types. The reconstructed function in (a) is identical to the continuous, band-limited original. The results for the step function (b) and the pulse function (c) show the strong ringing caused by Sinc (ideal low-pass) interpolation.

maximum signal bandwidth but, on the other hand, also delivers a good reconstruction at rapid signal transitions. In this regard, the Sinc function is an extreme choice—it implements an ideal low-pass filter and thus preserves a maximum bandwidth and signal continuity but gives inferior results at signal transitions. At the opposite extreme, nearest-neighbor interpolation (see Fig. 22.2) can perfectly handle steps and pulses but generally fails to produce a continuous signal reconstruction between sample points. The design of an interpolation function thus always involves a trade-off, and the quality of the results often depends on the particular application and subjective judgment. In the following, we discuss some common interpolation functions that come close to this goal and are therefore frequently used in practice.

22.2 Interpolation by Convolution

As we saw earlier in the context of Sinc interpolation (Eqn. (22.5)), the reconstruction of a continuous signal can be described as a linear convolution operation. In general, we can express interpolation as a convolution of the given discrete function $g(u)$ with some continuous *interpolation kernel* $w(x)$ as

$$\tilde{g}(x_0) = [w * g](x_0) = \sum_{u=-\infty}^{\infty} w(x_0 - u) \cdot g(u). \tag{22.8}$$

The Sinc interpolation in Eqn. (22.6) is obviously only a special case with $w(x) = \mathrm{Sinc}(x)$. Similarly, the 1D *nearest-neighbor interpolation* (Eqn. (22.1), Fig. 22.2(a)) can be expressed as a linear convolution with the kernel

$$w_{\mathrm{nn}}(x) = \begin{cases} 1 & \text{for } -0.5 \le x < 0.5, \\ 0 & \text{otherwise,} \end{cases} \tag{22.9}$$

and the *linear interpolation* (see Eqn. (22.2), Fig. 22.2(b)) with the kernel

$$w_{\mathrm{lin}}(x) = \begin{cases} 1 - |x| & \text{for } |x| < 1, \\ 0 & \text{for } |x| \ge 1. \end{cases} \tag{22.10}$$

Both interpolation kernels $w_{\mathrm{nn}}(x)$ and $w_{\mathrm{lin}}(x)$ are shown in Fig. 22.7, and results for various function types are plotted in Fig. 22.8.

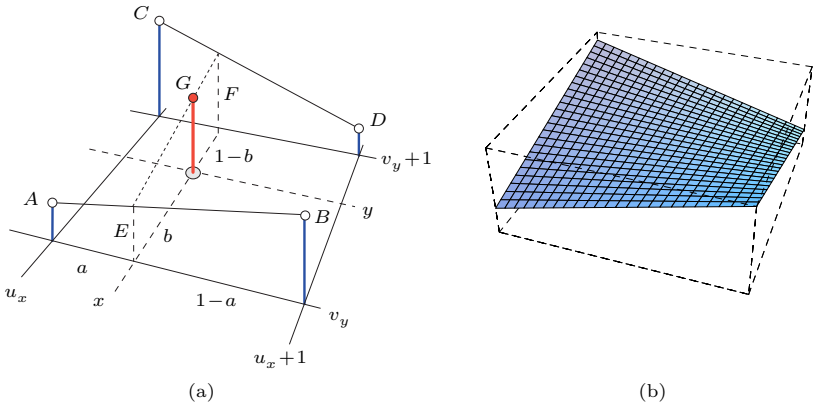

Fig. 22.17 Bilinear interpolation. For a given position (x, y), the interpolated value is computed from the values A, B, C, D of the four closest pixels in two steps (a). First the intermediate values E and F are computed by linear interpolation in the horizontal direction between A, B and C, D, respectively, where $a = x - u_x$ is the distance to the nearest pixel to the left of x. Subsequently, the intermediate values E, F are interpolated in the vertical direction, where $b = y - v_y$ is the distance to the nearest pixel below y. An example for the resulting surface between four adjacent pixels is shown in (b).

where $u_x = \lfloor x \rfloor$ and $v_x = \lfloor y \rfloor$. Then the pixel values A, B, C, D are interpolated in horizontal and subsequently in vertical direction. The intermediate values E, F are calculated from the distance $a = (x - u_x)$ of the specified interpolation position (x, y) from the discrete raster coordinate u_x as

$$E = A + (x - u_x) \cdot (B - A) = A + a \cdot (B - A), \tag{22.31}$$
$$F = C + (x - u_x) \cdot (D - C) = C + a \cdot (D - C), \tag{22.32}$$

and the final interpolation value G is computed from the vertical distance $b = y_0 - v_y$ as

$$\begin{aligned} \tilde{I}(x, y) = G &= E + (y - v_y) \cdot (F - E) = E + b \cdot (F - E) \\ &= (a-1)(b-1)\, A + a(1-b)\, B + (1-a)\, b\, C + a\, b\, D\,. \end{aligned} \tag{22.33}$$

Expressed as a linear convolution filter, the corresponding 2D kernel $W_{\text{bil}}(x, y)$ is the product of the two 1D kernels $w_{\text{lin}}(x)$ and $w_{\text{lin}}(y)$ (Eqn. (22.10)), that is,

$$\begin{aligned} W_{\text{bilin}}(x, y) &= w_{\text{lin}}(x) \cdot w_{\text{lin}}(y) \\ &= \begin{cases} 1 - |x| - |y| + |x \cdot y| & \text{for } 0 \le |x|, |y| < 1, \\ 0 & \text{otherwise.} \end{cases} \end{aligned} \tag{22.34}$$

In this function (plotted in Fig. 22.18 (a)), we can recognize the bilinear term that gives this method its name.

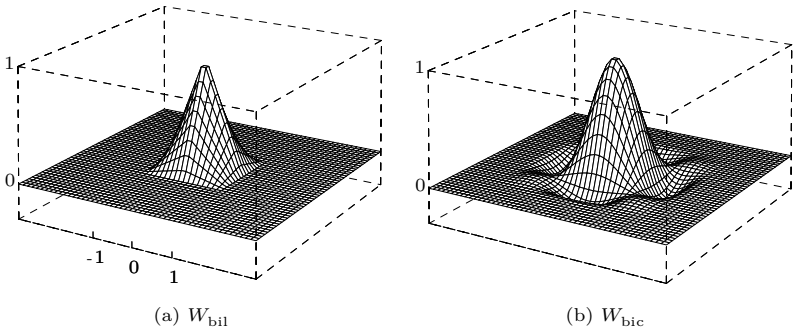

(a) W_{bil} (b) W_{bic}

Fig. 22.18 2D interpolation kernels. Bilinear kernel $W_{\text{bil}}(x, y)$ (a) and bicubic kernel $W_{\text{bic}}(x, y)$ (b) for $-3 \le x, y \le 3$.

for $a, b \in \mathbb{R}$. This type of operator or library method was not available in the standard Java API until recently.[2] The following Java method implements the mod operation according to the definition in Eqn. (F.1):[3]

```
int Mod(int a, int b) {
  if (b == 0)
    return a;
  if (a * b >= 0 || a % b == 0) {   ← error fixed!
    return a - b * (a / b);
  else
    return a - b * (a / b - 1);
}
```

Note that the *remainder* operator `%`, defined as

$$a \,\%\, b \;\equiv\; a - b \cdot \text{truncate}(a/b), \qquad \text{for } b \neq 0, \tag{F.2}$$

is often used in this context, but yields the same results only for *positive* operands $a \geq 0$ and $b > 0$. For example,

$$\begin{array}{rcrcr} 13 & \text{mod} & 4 & = & 1 \\ 13 & \text{mod} & -4 & = & -3 \\ -13 & \text{mod} & 4 & = & 3 \\ -13 & \text{mod} & -4 & = & -1 \end{array} \quad \text{vs.} \quad \begin{array}{rcrcr} 13 & \,\%\, & 4 & = & 1 \\ 13 & \,\%\, & -4 & = & 1 \\ -13 & \,\%\, & 4 & = & -1 \\ -13 & \,\%\, & -4 & = & -1 \end{array}$$

F.1.3 Unsigned Byte Data

Most grayscale and indexed images in Java and ImageJ are composed of pixels of type `byte`, and the same holds for the individual components of most color images. A single byte consists of eight bits and can thus represent $2^8 = 256$ different bit patterns or values, usually mapped to the numeric range $0, \ldots, 255$. Unfortunately, Java (unlike C and C++) does *not* provide a suitable "unsigned" 8-bit data type. The primitive Java type `byte` is "signed", using one of its eight bits for the $\pm$ sign, and is intended to hold values in the range $-128, \ldots, +127$.

Java's `byte` data can still be used to represent the values 0 to 255, but conversions must take place to perform proper arithmetic computations. For example, after execution of the statements

```
int  a = 200;
byte b = (byte) p;
```

the variables `a` (32-bit `int`) and `b` (8-bit `byte`) contain the binary patterns

```
a = 00000000000000000000000011001000
b =                         11001000
```

Interpreted as a (signed) `byte` value, with the leftmost bit[4] as the sign bit, the variable `b` has the decimal value -56. Thus after the statement

[2] Starting with Java version 1.8 the mod operation (as defined in Eqn. (F.1)) is implemented by the standard method `Math.floorMod(a, b)`.
[3] The definition in Eqn. (F.1) is not restricted to integer operands.
[4] Java uses the standard "2s-complement" representation, where a sign bit = 1 stands for a negative value.